

12-16-2015

Dynamics of Density Cavities Generated by Frictional Heating: Formation, Distortion, and Instability

M. D. Zettergren

Embry-Riddle Aeronautical University, zettergm@erau.edu

J. L. Semeter

Boston University

H. Dahlgren

Royal Institute of Technology KTH,

Follow this and additional works at: <https://commons.erau.edu/publication>

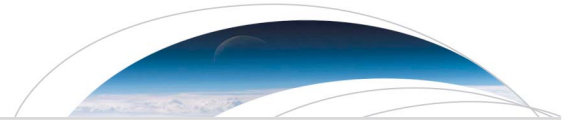


Part of the [Atmospheric Sciences Commons](#)

Scholarly Commons Citation

Zettergren, M. D., Semeter, J. L., & Dahlgren, H. (2015). Dynamics of Density Cavities Generated by Frictional Heating: Formation, Distortion, and Instability. *Geophysical Research Letters*, 42(23).
<https://doi.org/10.1002/2015GL066806>

This Article is brought to you for free and open access by Scholarly Commons. It has been accepted for inclusion in Publications by an authorized administrator of Scholarly Commons. For more information, please contact commons@erau.edu.



RESEARCH LETTER

10.1002/2015GL066806

Key Points:

- Density cavities develop asymmetrically due to convection associated with strong frictional heating
- Aurorally generated ionospheric density cavities might be susceptible to gradient-drift instability
- Ionospheric density cavities also likely experience mesoscale distortion due to drifts

Supporting Information:

- Supporting Information S1
- Movie S1

Correspondence to:

M. D. Zettergren,
zettergm@erau.edu

Citation:

Zettergren, M. D., J. L. Semeter, and H. Dahlgren (2015), Dynamics of density cavities generated by frictional heating: Formation, distortion, and instability, *Geophys. Res. Lett.*, 42, 10,120–10,125, doi:10.1002/2015GL066806.

Received 29 OCT 2015

Accepted 16 NOV 2015

Accepted article online 20 NOV 2015

Published online 11 DEC 2015

Dynamics of density cavities generated by frictional heating: Formation, distortion, and instability

M. D. Zettergren¹, J. L. Semeter², and H. Dahlgren^{3,4}

¹Department of Physical Sciences and Center for Space and Atmospheric Research, Embry-Riddle Aeronautical University, Daytona Beach, Florida, USA, ²Department of Electrical and Computer Engineering and Center for Space Physics, Boston University, Boston, Massachusetts, USA, ³Space Plasma Physics, KTH Royal Institute of Technology, Stockholm, Sweden, ⁴Space Environment Physics, University of Southampton, Southampton, UK

Abstract A simulation study of the generation and evolution of mesoscale density cavities in the polar ionosphere is conducted using a time-dependent, nonlinear, quasi-electrostatic model. The model demonstrates that density cavities, generated by frictional heating, can form in as little as 90 s due to strong electric fields of ~ 120 mV/m, which are sometimes observed near auroral zone and polar cap arcs. Asymmetric density cavity features and strong plasma density gradients perpendicular to the geomagnetic field are naturally generated as a consequence of the strong convection and finite extent of the auroral feature. The walls of the auroral density cavities are shown to be susceptible to large-scale distortion and gradient-drift instability, hence indicating that arc-related regions of frictional heating may be a source of polar ionospheric density irregularities.

1. Introduction

A wide variety of high-latitude ionospheric processes contribute to *E* and *F* region density depletions, here termed cavities. Strong $\mathbf{E} \times \mathbf{B}$ drifts (in excess of ~ 1 km/s) cause intense frictional heating through ion-neutral collisions. Resulting high temperatures (~ 2000 – 5000 K) modify chemical reaction rates that convert *F* region O^+ to molecular ions, which then recombine quickly [e.g., Schunk *et al.*, 1975]. In auroral downward current regions, divergent *E* region Pedersen drifts can create deep density depletions that may also extend into the lower *F* region [Doe *et al.*, 1995; Karlsson *et al.*, 2005]. Recent modeling efforts have focused on the synergistic effects of these two processes acting in concert with type-1 ion up flows [Wahlund *et al.*, 1992] and have shown that these are all likely to be significant in auroral arc downward current regions [Zettergren and Semeter, 2012].

Observational efforts, particularly from incoherent scatter radar (ISR) measurements, have been used in the past to demonstrate the occurrence of density cavities in close proximity to auroras [Doe *et al.*, 1993; Aikio *et al.*, 2004]. More recent experiments have leveraged the electronic steering capabilities of the PFISR (Poker Flat Incoherent Scatter Radar) system to image some features of mesoscale density cavities (roughly ~ 100 km by 200 – 500 km size) and establish their relation to regions of downward current and strong ion heating [Zou *et al.*, 2013; Zettergren *et al.*, 2014]. Ionospheric observations in the polar cap have demonstrated existence of moving polar cap arcs [Koustov *et al.*, 2012], while studies using the Resolute Bay incoherent scatter radar (RISR) have shown that moving density cavities can form alongside these types of arcs [Perry *et al.*, 2015].

The evolution of plasma density structures subjected to $\mathbf{E} \times \mathbf{B}$ drifts has been studied in the context of polar cap patches and smaller-scale barium release-generated plasma clouds. It is well known that both types of density enhancements can become unstable where there is an *F* region density gradient along the drift direction [Tsunoda, 1988] (the gradient-drift instability (GDI)). This instability results in production of striations and structures at smaller scales from seed perturbations within the density gradient. These structures are of general interest as they can significantly impact radio communications (producing, e.g., HF backscatter and scintillation). Modeling studies of GDI have shown that both the presence of large *E* region conductances and polarization drifts can suppress the instability and affect the final state of the small-scale density structures [e.g., Mitchell *et al.*, 1985a; Gondarenko and Guzdar, 1999]. Polarization drifts and attendant shear-related instabilities have also been shown to impact the spectrum of density irregularities produced from a polar cap patch structure [Gondarenko and Guzdar, 2006, and references therein]. Drifting, spatially finite plasma clouds

may be susceptible to GDI and also have a tendency to elongate in the drift direction over time due to internal polarization electric fields [e.g., *Mitchell et al.*, 1985b, and references therein].

The present work examines the formation of high-latitude density *cavities* and their subsequent evolution in the presence of magnetospherically applied electric fields. This situation appears consistent with many recent imaging measurements of these structures and may be expected to occur in the vicinity of auroral zone and polar cap arcs. Particular focus is given to the three-dimensional structure of density cavities during formation, and the degree to which cavities become susceptible to subsequent structuring processes (GDI, convective distortion, etc.) noted in prior studies of plasma density enhancements. It seems reasonable to expect that aurorally formed density cavities may become unstable or exhibit larger-scale distortion. However, this process has not been carefully explored even though it appears that it may be relevant to recent observations. This study leverages an ionospheric transport model to quantitatively evaluate: (1) three-dimensional responses and structure of a forming density cavity, (2) the efficiency of auroral density cavitation at producing gradients susceptible to GDI, and (3) effects of cavity finiteness, including convective distortion similar to that noted in plasma cloud studies.

2. Modeling Approach

The model used in this study is based on *Zettergren and Semeter* [2012] and solves dynamic conservation of mass, parallel momentum, and energy equations for six ion species s ($s = O^+, NO^+, N_2^+, O_2^+, N^+, H^+$). Continuity equations include all chemical reactions relevant to the E , F , and topside regions, as well as impact ionization sources based on calculations from *Fang et al.* [2008]. For electrons, the density is calculated using quasi-neutrality and the parallel velocity is computed from the parallel current density. A full electron energy equation, including the effects of heat fluxes from conduction and thermoelectric processes and inelastic cooling processes [*Schunk and Nagy*, 1978], is solved alongside the ion systems. The model uses a Cartesian, three-dimensional domain with a vertical magnetic field. The neutral atmosphere is taken from the MSIS-00 model [*Picone et al.*, 2002].

Perpendicular components of the momentum equations are solved with a steady state force balance approximation, as described in *Zettergren and Semeter* [2012]. Electric fields are found by enforcing a divergence-free current density, where the current is assumed to consist of both conduction currents (directly dependent on the electric field through the usual ionospheric Ohm's law) and polarization currents (from a spatiotemporally varying electric field) [cf. *Mitchell et al.*, 1985a; *Gondarenko and Guzdar*, 1999, and references therein]. In essence, this approach assumes that the behavior of the ionospheric response currents is, to leading order, electrostatic. These currents, however, are modified by a correction which accounts for polarization currents from slowly varying field structures. Hence, the ionospheric electric field is approximated by $\mathbf{E} = -\nabla\Phi$. Further assuming that the geomagnetic field lines are equipotentials and employing a field line integration yields an equation that can be solved for the electric potential, hence field

$$\nabla_{\perp} \cdot (\boldsymbol{\Sigma}_{\perp} \cdot \nabla_{\perp} \Phi) + \nabla_{\perp} \cdot \left[C_M \left(\frac{\partial}{\partial t} + \mathbf{v}_{\perp} \cdot \nabla_{\perp} \right) (\nabla_{\perp} \Phi) \right] = \nabla_{\perp} \cdot (\boldsymbol{\Sigma}_{\perp} \cdot \mathbf{E}_{0\perp}). \quad (1)$$

In this equation Φ is the electric potential generated by the ionospheric response to a magnetospherically imposed electric field $\mathbf{E}_{0\perp}$ and $\mathbf{v}_{\perp} = (\mathbf{E}_{0\perp} - \nabla\Phi) \times \mathbf{B} / B^2$. $\boldsymbol{\Sigma}_{\perp}$ is the field line-integrated conductance tensor, and C_M is the inertial capacitance defined, e.g., in *Mitchell et al.* [1985a]. Note that equation (1) implicitly enforces the condition that all current closes within the ionosphere through either conduction currents or polarization currents (viz., no field-aligned current flow through the top boundary). Polarization currents generally suppress GDI growth through nonlocal closure of currents, similar in effect to shorting out of GDI through a strongly conducting E region.

For our field-integrated model, the top boundary FAC (Field-aligned current, assumed zero in equation (1)) must be specified. In a field-resolved model, one could alternatively specify potential at the top boundary. The obvious choice for topside potential would then be zero, which would tend to allow most excess charge to flow through the top boundary. This would have the effect of mostly preventing GDI growth and is inconsistent with numerous observations of small-scale plasma density structures in regions of density gradients. Moreover, this type of boundary condition presumes (incorrectly) that the overlying ionosphere-magnetosphere can close any amount of field-aligned current generated in the ionosphere. A zero FAC topside boundary condition, which is enforceable in either our field-integrated model or a

field-resolved model, has the possibility of over-accentuating GDI growth by not allowing FACs to carry excess charge through the top boundary (current still closes through the E region and polarization drifts). However, it still appears to represent the best option for use with this type of model.

Equation (1) is solved by employing a direct LU factorization via the MUMPS software package [Amestoy *et al.*, 2001, 2006]. Some studies of gradient drift instability have suggested that a field-resolved potential solution suppresses the growth of longer wavelength modes, hence, resulting in a different spectrum of density fluctuations [e.g. Guzdar *et al.*, 1998]. Recent studies of other gradient-generated instabilities (e.g., gravitational Rayleigh-Taylor (GRTI)) have employed three-dimensional potential solutions, with fewer cells than used here and suggested differences from a field-integrated formulation [Keskinen *et al.*, 2003; Aveiro and Hysell, 2012; Hysell *et al.*, 2014]. Other studies indicate that the GRTI growth rates may not be greatly affected by a field-integrated formulation, but the details of the structures formed by the instabilities differ somewhat [Aveiro and Huba, 2013]. High-resolution, three-dimensional, nonperiodic potential solutions are not possible with our current computational resources. However, we have conducted comparisons of field-integrated and field-resolved potential solutions at low resolution. Results indicate only minor differences in the GDI-generated density structures in scenarios similar to those studied in this paper.

Both the potential and electric field are assumed to go to zero at the x and y boundaries. This condition is restrictive and necessitates that boundary surfaces be far from the modeled density cavities. An appropriate boundary distance is found by running the model, at a reduced resolution, with the boundaries placed at different distances.

3. Modeled Ionospheric Density Cavity Dynamics

For the present simulations, a grid of size $N_z \times N_x \times N_y = 64 \times 600 \times 1000$ cells is used to cover the region $80 \leq z \leq 1000$ km, $-1000 \leq x \leq 1000$ km, and $-1000 \leq y \leq 1000$ km. Initial conditions for the simulation are a horizontally homogeneous ionosphere with $N_m F_2 \approx 5 \times 10^{11} \text{ m}^{-3}$. Background precipitation which is constant in space and time is applied throughout the simulation. This precipitation has a total energy flux of $5 \times 10^{-5} \text{ mW/m}^2$, which produces an E region with $N_m E \approx 3 \times 10^8 \text{ m}^{-3}$.

Each simulation results from a two-step driving process. First, a fixed potential pattern, shown in Figure 1a, is applied to the ionosphere for 90 s to generate an auroral density cavity. Ionospheric transport in the model is evolved self-consistently during this part of the simulation so that the cavity has realistic densities and spatial structure. The potential, which is seeded with small-scale variations (illustrated in Figure 1b, $\sim 1\%$ in the $y=0$ plane), results in an electric field with maximum of ~ 120 mV/m (producing a maximum drift of ~ 2.25 km/s). The basic structure of the density cavity, along the $y=0$ line after 90 s, is also shown in Figure 1b. In the second part of the simulation ($90 < t \leq 990$ s), a fixed, uniform background electric field ($\mathbf{E}_{0\perp} = -25 \hat{\mathbf{e}}_x$ mV/m) is applied for 900 s and self-consistent transport and electrodynamic responses (equation (1)) are solved. This causes the density cavity, which is surrounded by a higher density, structureless ionosphere, to drift and generate response electric fields. In order to isolate the ability of the cavity to produce GDI, electron precipitation (aside from the very weak background flux) is *not* applied in this simulation.

Three-dimensional ionospheric convection greatly impacts the production and structure of the cavity. Figure 2 shows ion temperature, NO^+ density, and plasma density in the $y = 0$ plane after the auroral electric field has been applied for 90 s. The arrows in this plot indicate plasma flows in the x - z plane (corresponding to the lengthwise and altitude dimensions of the cavity). High ion temperatures (Figure 2a), driven by fast drifts through the neutral atmosphere (assumed stationary) and frictional heating, generate large concentrations of molecular ions in the 200–300 km altitude range (Figure 2b). These molecular ions recombine over ~ 1 min time scales, generating a density cavity (Figure 2c). The cavity is displaced in the downstream direction from the center of the heating region. Ion upflows reaching vertical speeds of ~ 0.8 km/s are evident, and along with the horizontal drifts, these form a local “fountain effect,” temporarily moving plasma from the upper F region into the topside ionosphere and toward the $+x$ direction.

The aurorally generated density cavity evolves significantly after formation, and the three-dimensional shape of the newly formed cavity determines, to a degree, subsequent drift responses. Figure 3 shows plots of electron density in the geomagnetic field-perpendicular (x - y) plane at an altitude of 300 km at times of 90 s (Figure 3a), 600 s (Figure 3b), and 990 s (Figure 3c). Arrows in Figures 3b and 3c indicate flow directions and magnitude relative to the $\mathbf{E}_{0\perp} \times \mathbf{B}$ drift. The black line in each plot indicates the cavity wall, defined as the

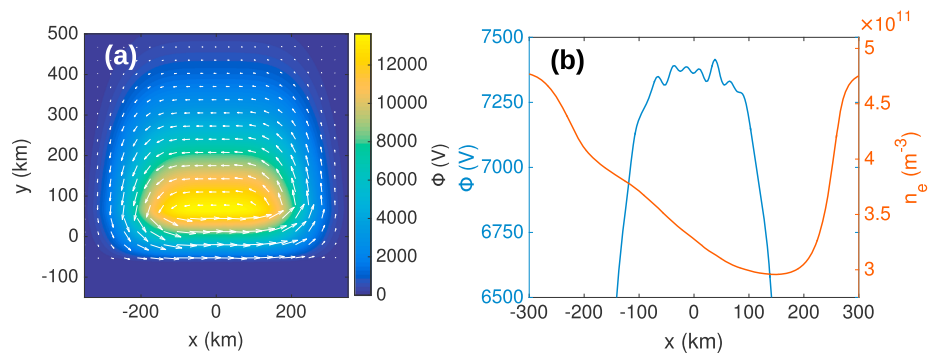


Figure 1. Potential pattern, flows, and seed structures used to generate an auroral density cavity. (a) The potential is shown by the background color map, and the arrows indicate the direction of the $\mathbf{E}_{0\perp} \times \mathbf{B}$ flow. The speed, which maximizes at about 2.25 km/s is indicated by the length of each arrow. (b) A zoomed-in view of the potential at $y = 0$, which illustrates seed structures. The density at $y = 0, z = 300$ km after 90 s is shown in Figure 1b to illustrate cavity structure.

location where the density is halfway in between that of the cavity and that of the surrounding plasma, and the y coordinate is centered on where the cavity would be if it undergoes purely $\mathbf{E}_{0\perp} \times \mathbf{B}$ drift. The basic structure of the density cavity after formation, discussed above, is apparent in Figure 3a. The density cavity is wider and more pronounced on its downstream (roughly $+x$) side due to convection of the depleted plasma as it forms. Strong gradients exist in density, and there are small-scale variations in position of the cavity wall (which seed the instability). After 510 s of evolution in the uniform 25 mV/m electric field (Figure 3b), GDI has initiated on the leading edge wall of the cavity. By 900 s (Figure 3c), some large-scale distortion has occurred, and the leading edge gradients have steepened. GDI tends to break the cavity up into narrow features along the direction of background flow. The GDI is most pronounced along the positive x side of the cavity, which has a stronger gradient following formation.

In addition to GDI other larger-scale drift responses exist. The cavity drifts slightly faster than $\mathbf{E}_{0\perp} \times \mathbf{B}$ speed, and its trailing edge becomes more diffuse with time (see density gradients around the trailing edge black line in Figures 3a and 3c). A large-scale distortion of lateral ends (at $x = \pm 225$) of cavity has also occurred by $t = 990$ s.

Figure 4 shows the response electric potential and charge density (a) and electric field (b) at 990 s. The total potential difference across the mesoscale cavity structure ($-200 \leq x \leq 300$ km) is ~ 650 V, and smaller-scale, intense potential structures associated with GDI are prevalent. Electric fields due to GDI reach ~ 10 mV/m and are most pronounced on the $+x$ direction side of the cavity. The part of the density cavity from $100 \leq x \leq 200$ km, $-300 \leq y \leq -500$ km exhibits a mesoscale electric field feature with intensity ~ 5 mV/m. This electric field feature contributes to overall distortion of the $+x$ side of the cavity through enhanced

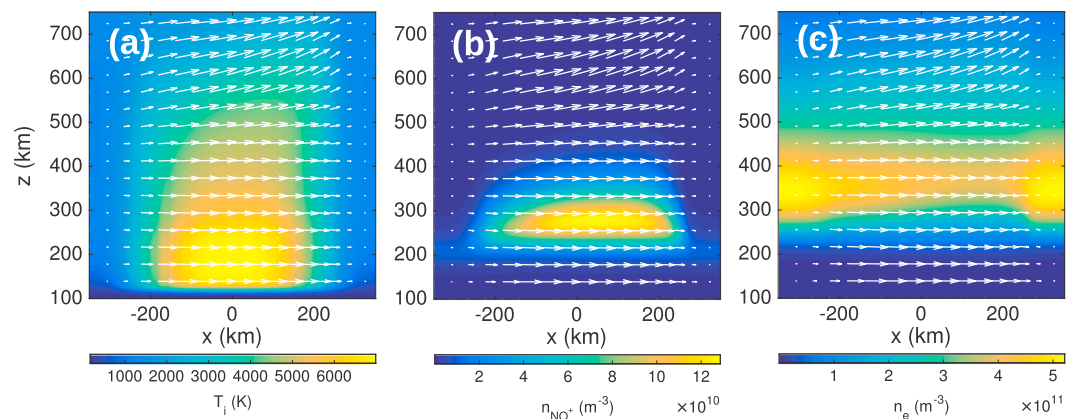


Figure 2. Plot of at (a) ion temperature, (b) NO^+ density, and (c) plasma density versus x and z at 90 s. White arrows indicate direction and magnitude of flows (length of arrow). The geomagnetic field-parallel component of these flows maximizes at about 0.8 km/s.

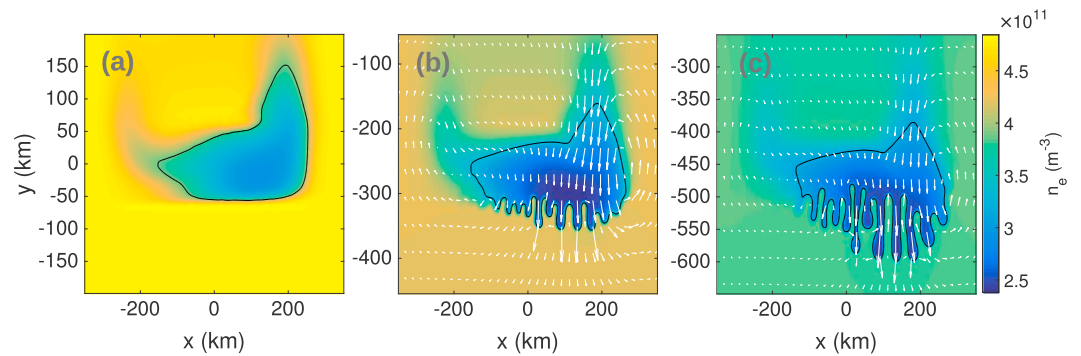


Figure 3. Electron density at 300 km altitude at three different times corresponding to (a) the end of the auroral disturbance (90 s), (b) after drifting due to a 25 mV/m background electric field for 510 s, and (c) after drifting for 900 s. Arrows in Figures 3b and 3c indicate the perpendicular velocity relative to the background $\mathbf{E}_{0\perp} \times \mathbf{B}$ drift ($v_y = -500$ m/s). This relative speed maximizes at ~ 200 m/s. The black contour in each plot represents the boundary of the density cavity; quantitatively, the location at which the density is halfway between the lowest cavity density and the background density. The y coordinate of each panel is shifted by the $\mathbf{E}_{0\perp} \times \mathbf{B}$ drift distance for each time frame to facilitate comparison.

response flows. A cavity-scale dipolar, polarization potential pattern around the cavity (see contour lines in Figure 4a) is responsible for the fact that the structure, as a whole, drifts slightly faster than the $\mathbf{E}_{0\perp} \times \mathbf{B}$ drift speed.

4. Concluding Remarks

Model results indicate that finite, electric field-generated density cavities can exhibit interesting drift responses, including cavity-scale distortion and GDI. These processes are known to exist in artificially generated plasma clouds and polar cap patches, respectively, and here their plausible existence in mesoscale density cavities is demonstrated for the first time. Structuring of density cavities is shown to be affected by the cavity formation process; i.e., simulations show that convection of the cavity during formation critically affects where it is most susceptible to GDI.

Density cavity formation and evolution illustrated herein could represent a significant mode by which high-latitude plasma structures form. This process would be distinct from well-known patch and blob structuring processes in that the cavities are generated by polar arc-related electric fields which are usually more prevalent during northward interplanetary magnetic field conditions. Interaction and coupling between cavity formation via frictional heating and subsequent drift distortion and instability may produce a rich variety of plasma density structures. Further modeling to examine the parameter space of these different drivers would be useful for characterizing cavity behavior as would adding in additional relevant physics, such as arc-related

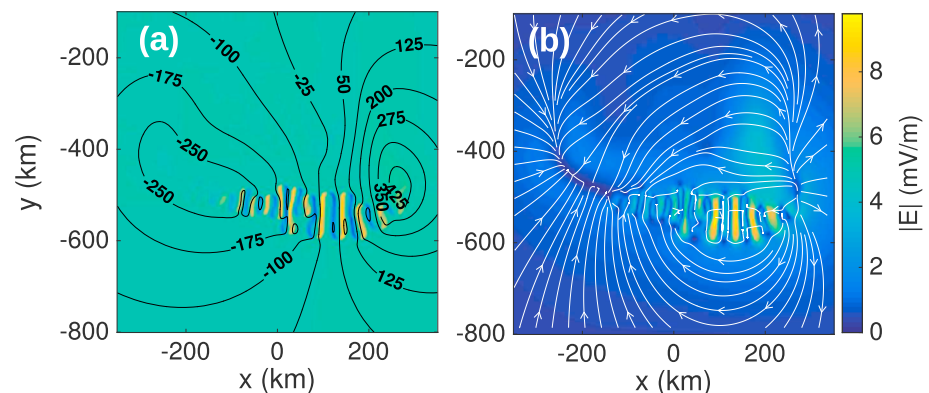


Figure 4. Electrodynamic parameters associated with cavity drift responses at 990 s. (a) Contours show equipotential lines, and the background color map qualitatively illustrates charge density (blue is negatively charged, yellow is positive, and green is neutral). (b) The direction of the electric field is shown as white arrows, and the magnitude of the field is shown as the background color map.

soft precipitation or a more sophisticated treatment of electrodynamics (fully 3-D potential solves and different specifications of boundary conditions). Moreover, case studies and systematic observations with the PFISR/RISR radar systems will be capable of determining how often cavities form in the polar cap and their potential to generate further structuring.

Acknowledgments

Research was supported by NSF grant AGS-1339537 to Embry-Riddle Aeronautical University. Models used in this study were developed under support from NSF CAREER grant AGS-1255181. This work also greatly benefitted from discussions during the ISSI small-scale electrodynamics workshop. Data used to generate plots are available upon request to the authors.

References

- Aikio, A., K. Mursula, S. Buchert, F. Forme, O. Amm, G. Marklund, M. Dunlop, D. Fontaine, A. Vaivads, and A. Fazakerley (2004), Temporal evolution of two auroral arcs as measured by the Cluster satellite and coordinated ground-based instruments, *Ann. Geophys.*, *22*, 4089–4101, doi:10.5194/angeo-22-4089-2004.
- Amestoy, P. R., I. S. Duff, J. Koster, and J.-Y. L'Excellent (2001), A fully asynchronous multifrontal solver using distributed dynamic scheduling, *SIAM J. Matrix Anal. Appl.*, *23*, 15–41.
- Amestoy, P. R., A. Guermouche, J.-Y. L'Excellent, and S. Pralet (2006), Hybrid scheduling for the parallel solution of linear systems, *Parallel Computing*, *32*(2), 136–156.
- Aveiro, H. C., and J. D. Huba (2013), Equatorial spread F studies using SAMI3 with two-dimensional and three-dimensional electrostatics, *Ann. Geophys.*, *31*, 2157–2162, doi:10.5194/angeo-31-2157-2013.
- Aveiro, H. C., and D. L. Hysell (2012), Implications of the equipotential field line approximation for equatorial spread F analysis, *Geophys. Res. Lett.*, *39*, L11106, doi:10.1029/2012GL051971.
- Doe, R. A., M. Mendillo, J. F. Vickrey, L. J. Zanetti, and R. W. Eastes (1993), Observations of nightside auroral cavities, *J. Geophys. Res.*, *98*, 293–310, doi:10.1029/92JA02004.
- Doe, R. A., J. F. Vickrey, and M. Mendillo (1995), Electrodynamic model for the formation of auroral ionospheric cavities, *J. Geophys. Res.*, *100*, 9683–9696, doi:10.1029/95JA00001.
- Fang, X., C. E. Randall, D. Lummerzheim, S. C. Solomon, M. J. Mills, D. R. Marsh, C. H. Jackman, W. Wang, and G. Lu (2008), Electron impact ionization: A new parameterization for 100 eV to 1 MeV electrons, *J. Geophys. Res.*, *113*, A09311, doi:10.1029/2008JA013384.
- Gondarenko, N. A., and P. N. Guzdar (1999), Gradient drift instability in high latitude plasma patches: Ion inertial effects, *Geophys. Res. Lett.*, *26*, 3345–3348, doi:10.1029/1999GL003647.
- Gondarenko, N. A., and P. N. Guzdar (2006), Nonlinear three-dimensional simulations of mesoscale structuring by multiple drives in high-latitude plasma patches, *J. Geophys. Res.*, *111*, A08302, doi:10.1029/2006JA011701.
- Guzdar, P. N., N. A. Gondarenko, P. K. Chaturvedi, and S. Basu (1998), Three-dimensional nonlinear simulations of the gradient drift instability in the high-latitude ionosphere, *Radio Sci.*, *33*, 1901–1913, doi:10.1029/98RS01703.
- Hysell, D. L., R. Jafari, D. C. Fritts, and B. Laughman (2014), Gravity wave effects on postsunset equatorial F region stability, *J. Geophys. Res. Space Physics*, *119*, 5847–5860, doi:10.1002/2014JA019990.
- Karlsson, T., G. Marklund, N. Brenning, and I. Aarnas (2005), On enhanced aurora and low-altitude parallel electric fields, *Phys. Scr.*, *72*, 419–422, doi:10.1238/Physica.Regular.072a00419.
- Keskinen, M. J., S. L. Ossakow, and B. G. Fejer (2003), Three-dimensional nonlinear evolution of equatorial ionospheric spread- F bubbles, *Geophys. Res. Lett.*, *30*, 1855, doi:10.1029/2003GL017418.
- Koustov, A. V., K. Hosokawa, N. Nishitani, K. Shiokawa, and H. Liu (2012), Signatures of moving polar cap arcs in the F -region PolarDARN echoes, *Ann. Geophys.*, *30*, 441–455, doi:10.5194/angeo-30-441-2012.
- Mitchell, H. G. Jr., J. A. Fedder, M. J. Keskinen, and S. T. Zalesak (1985a), A simulation of high latitude F -layer instabilities in the presence of magnetosphere-ionosphere coupling, *Geophys. Res. Lett.*, *12*, 283–286, doi:10.1029/GL012i005p00283.
- Mitchell, H. G. Jr., J. A. Fedder, J. D. Huba, and S. T. Zalesak (1985b), Transverse motion of high-speed barium clouds in the ionosphere, *J. Geophys. Res.*, *90*, 11,091–11,095, doi:10.1029/JA090iA11p11091.
- Perry, G. W., H. Dahlgren, M. J. Nicolls, M. Zettergren, J.-P. St.-Maurice, J. L. Semeter, T. Sundberg, K. Hosokawa, K. Shiokawa, and S. Chen (2015), Spatiotemporally resolved electrodynamic properties of a Sun-aligned arc over Resolute Bay, *J. Geophys. Res. Space Physics*, *120*, doi:10.1002/2015JA021790.
- Picone, J. M., A. E. Hedin, D. P. Drob, and A. C. Aikin (2002), NRLMSISE-00 empirical model of the atmosphere: Statistical comparisons and scientific issues, *J. Geophys. Res.*, *107*, 1468, doi:10.1029/2002JA009430.
- Schunk, R. W., and A. F. Nagy (1978), Electron temperatures in the F region of the ionosphere—Theory and observations, *Rev. Geophys.*, *16*, 355–399.
- Schunk, R. W., P. M. Banks, and W. J. Raitt (1975), Effect of electric fields on the daytime high-latitude E and F regions, *J. Geophys. Res.*, *80*, 3121–3130.
- Tsunoda, R. T. (1988), High-latitude F region irregularities—A review and synthesis, *Rev. Geophys.*, *26*, 719–760, doi:10.1029/RG026i004p00719.
- Wahlund, J.-E., H. J. Opgenoorth, I. Häggström, K. J. Winser, and G. O. L. Jones (1992), EISCAT observations of topside ionospheric ion outflows during auroral activity: Revisited, *J. Geophys. Res.*, *97*, 3019–3037.
- Zettergren, M., and J. Semeter (2012), Ionospheric plasma transport and loss in auroral downward current regions, *J. Geophys. Res.*, *117*, A06306, doi:10.1029/2012JA017637.
- Zettergren, M., K. Lynch, D. Hampton, M. Nicolls, B. Wright, M. Conde, J. Moen, M. Lessard, R. Miceli, and S. Powell (2014), Auroral ionospheric F region density cavity formation and evolution: MICA campaign results, *J. Geophys. Res. Space Physics*, *119*, 3162–3178, doi:10.1002/2013JA019583.
- Zou, S., M. B. Moldwin, M. J. Nicolls, A. J. Ridley, A. J. Coster, E. Yizengaw, L. R. Lyons, and E. F. Donovan (2013), Electrodynamics of the high-latitude trough: Its relationship with convection flows and field-aligned currents, *J. Geophys. Res. Space Physics*, *118*, 2565–2572, doi:10.1002/jgra.50120.